

# Experimental Analysis of the nonlinear Vibrations of a rigid Rotor in Gas Foil Bearings

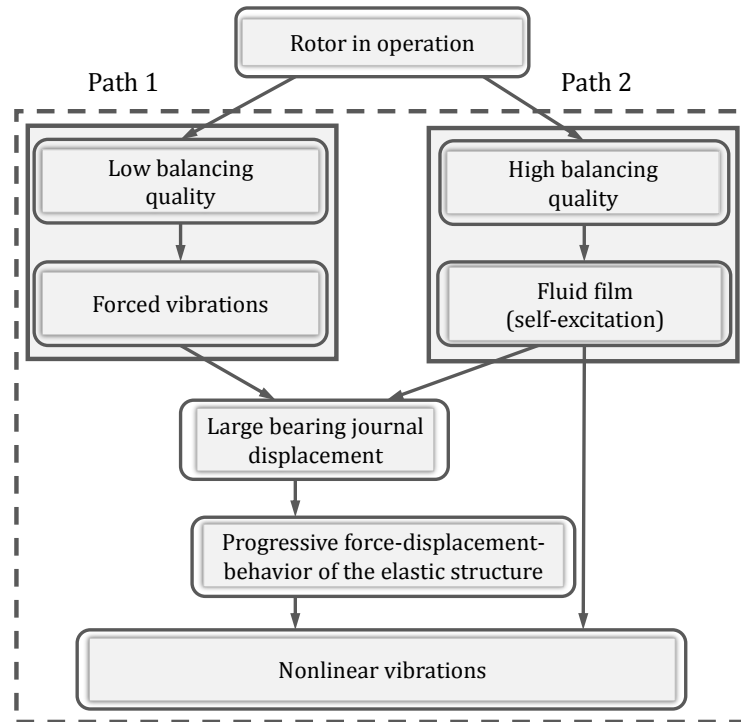
Robert Hoffmann, Cédric Kayo, Robert Liebich

*Air bearings and gas foil bearings (GFBs) in particular are characterized by a low-loss operation at high rotational speeds and temperatures, because of their adequate and relatively low lubrication viscosity. Further advantages are the simple design of the bearing and the omission of an oil system. A disadvantage is the low fluid viscosity, which limits the load capacity and damping capacity of the bearing. Even though the bearing wall, which is elastic and sensitive to friction, compensates the mentioned disadvantages by self-regulating the lubrication film and providing external damping. GFBs always show a tendency for nonlinear subharmonic vibrations. In this paper, the nonlinear vibration behavior of a rigid rotor in gas foil bearings is investigated. The rotor is accelerated to approx. 60 000 rpm by means of an impulse turbine. Waterfall charts for a variation of static and dynamic unbalance are recorded using transient coast-downs. The experiments show a variety of nonlinear effects. Their causes are analyzed experimentally. In addition to self-excitation by the fluid film, the rotor is sensitive to high unbalances and the resulting forced vibrations. The nonlinear, progressive system behavior results in excitation orders of  $1/2\Omega$ ,  $1/3\Omega$ , and  $1/4\Omega$  that modulate additional frequencies.*

## 1 Introduction

Gas foil bearings (GFBs) are based on a fluid dynamic lubrication principle and possess a variety of benefits. Due to the use of ambient air, a conventional oil system is not necessary. At the same time, losses in the lubrication film are relatively low and high temperature applications are possible, which can be explained by the relatively low viscosity and the thermal behavior of gases. Nonetheless, a low viscosity results in low load capacity and poor damping properties. Apart from the external damping caused by friction in the foils, the elastic structure forms a self-regulating lubrication film, cf. Heshmat (1994). The latter particularly increases the load capacity when compared to rigid gas bearings, cf. DellaCorte and Valco (2000). However, systems with GFB-supported systems often manifest nonlinear subharmonic vibrations, cf. Heshmat (1994, 2000); Kim et al. (2010); Kim (2007); Sim et al. (2012); Larsen (2015). If the damping of the system is sufficiently large there are stable limit cycles, Kim (2007); Heshmat (1994). Moreover, the unbalance of the system significantly influences the nonlinear vibration behavior, Heshmat et al. (1982); San Andrés et al. (2007); Kim (2007); San Andrés and Kim (2008); Balducchi (2013); Larsen (2015). Despite the large number of experimental rotordynamic investigations, no detailed classification of the vibration is available. In 2007, San Andrés and Kim (2008) labeled the nonlinear behavior as *Forced Nonlinearity*, which is influenced by the unbalance, whereby self-excitation has been completely excluded. Instead, Hoffmann et al. (2014) proved numerically the possibility of self-excitation in a nonlinear stability analysis. Consequently, in well balanced systems the subharmonic vibration starts at the rotational speed  $n_{OSSV}$  (*Onset Speed of Subharmonic Vibration*) and vibrates synchronously with the eigenfrequency of the system. The onset of subharmonic vibration is characterized by a Hopf-bifurcation resulting from a fluid film induced self-excitation. A possible classification of the nonlinear vibrations of a rotor in a GFB is displayed in Figure 1. The system behavior can take one of two paths: forced vibration and self-excited vibration.

## 1.1 Path 1: Forced Vibration



**Figure 1:** Classification of the vibration characteristic of a GFB mounted system

The generation of nonlinear vibration in path 1 is due to forced vibrations caused by poor balancing quality. Due to the progressive force-displacement-behavior of a gas foil bearing, the system behaves similarly to a Duffing-oscillator, cf. Yamamoto and Ishida (2001); Kovacic and Brennan (2011); Dresig et al. (2011); Magnus et al. (2013). The Duffing equation (Equation 1) is a differential equation for a damped elastic structure subjected to a large deformation, where  $m$  is the mass of the system,  $\Omega$  the rotor speed,  $\delta$  the damping coefficient and  $r(x)$  the nonlinear elastic restoring forces.

$$\ddot{x} + 2\delta\dot{x} + r(x) = F \cos(\Omega t) \quad (1)$$

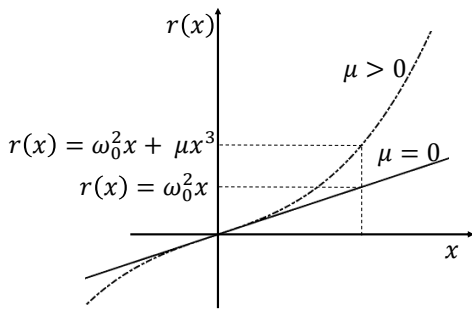
The nonlinear forces are induced by the elastic structure of the GFB and the gas film. The large displacement of the shaft in the bearing makes nonlinear elastic effects significant (Figure 2). Figure 3 shows the response amplitude of the Duffing equation by applying the harmonic balance method and assuming a solution of the form (Equation 2).

$$x_1(t) = C \sin(\Omega t + \varphi) \quad (2)$$

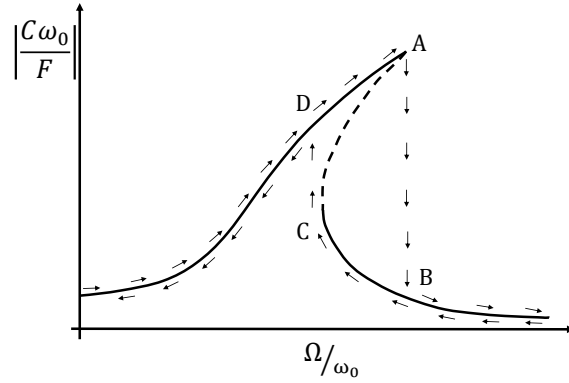
One particularity of the duffing oscillator is the jump phenomenon in the resonance peak of the frequency response function, which occurs when the system is excited by a harmonic force (Figure 3). When the frequency of excitation increases, there appears suddenly a jump down from point (A) to (B). If the frequency decreases, the amplitude jumps up from point (C) to (D). This phenomenon can be observed during the experiment (chapter 3). Jump phenomena, subharmonic resonances of the  $1/2\Omega$ ,  $1/3\Omega$  and  $1/4\Omega$  etc. order and frequency modulations are characteristics of such an oscillator, cf. Yamamoto and Ishida (2001); Kovacic and Brennan (2011).

## 1.2 Path 2: Self-excited Vibration

Nevertheless, a very well balanced rotor can also exhibit nonlinear vibrations during operation. The cause is fluid-induced, self-excited vibrations by the air lubrication (Whirl-vibration). At the OSSV-point, subharmonic fractions rise and vibrate synchronously with a system eigenfrequency. Due to the large displacements of the shaft, the progressive behavior of the bearing comes into effect, so that ultimately a mixture of path 1 and 2 occurs. The purpose of this work is the experimental rotordynamic analysis of a rotor supported by GFBs focusing on its nonlinear vibration and the classification of the same according to the scheme from Figure 1.



**Figure 2:** Nonlinear stiffness



**Figure 3:** Frequency response of the resonant Duffing equation

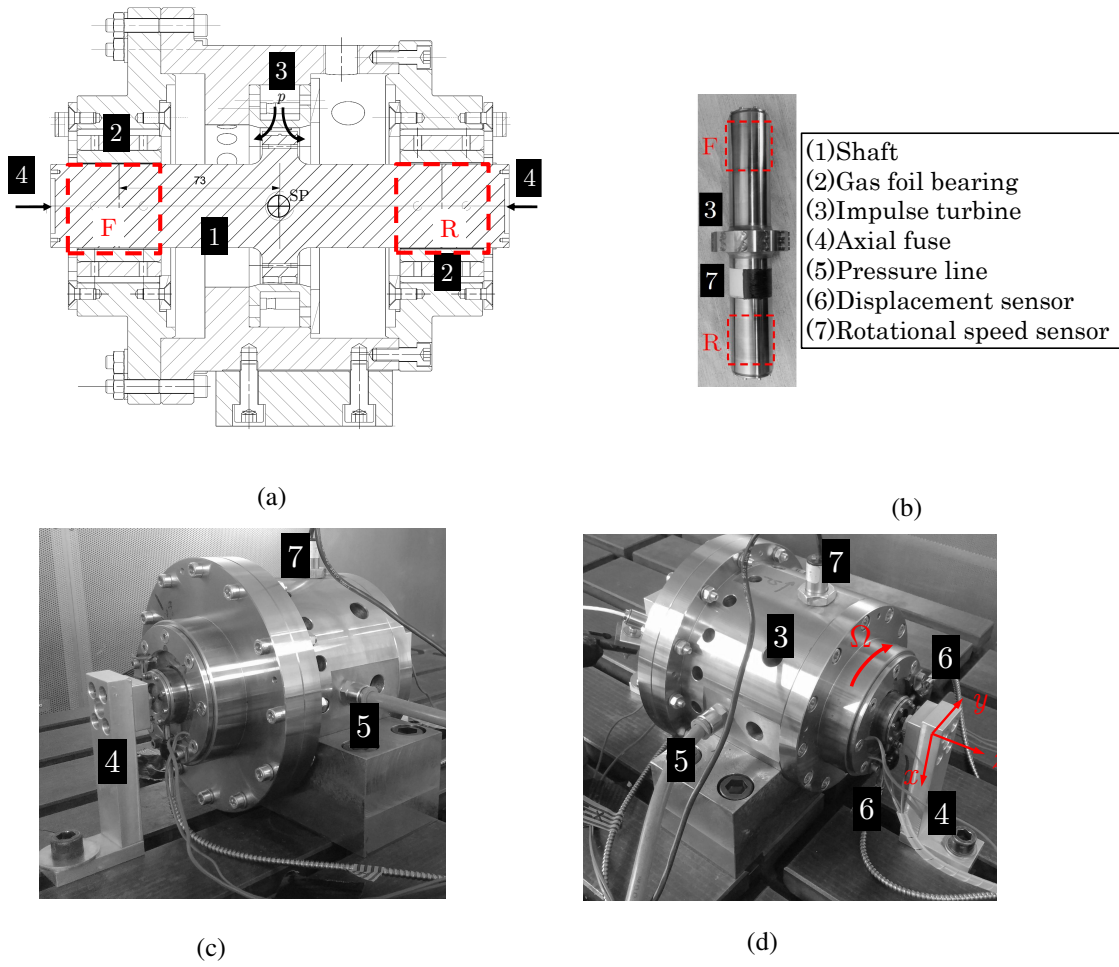
## 2 Experimental Setup

Figure 4 (a)-(d) presents the experimental setup for the rotordynamic analysis in a section view (a) and in two further views (c) and (d). The cylindrical casing consists of precision turned components, so that a coaxial bearing seat is provided for the front (F) and rear (R), see Figure 4 (a). Two identically constructed radial GFBs of the 1st generation are investigated whose technical data are listed in Table 1. The mounting position of the bearing allows the rigid clamping of the foils (WP) to be at the 12 o'clock position and the bearing shaft to rotate from the free foil ending to the rigid clamp. The chassis is tightly connected to a vibration-isolated machine bed by means of a bracket. A numerical FE based modal analysis of the chassis structure shows no eigenfrequencies below 110 000 rpm, therefore no influence from the chassis at the operation range ( $n_{\max} \approx 60\,000$  rpm) is to be expected. The rigid rotor is driven by an impulse turbine (3) supplied with pressurized air, see Figure 4 (a) and (b), whose technical data can be found in Table 2. The rotor including the turbine is built symmetrically around the center of gravity (SP). Thus, similar radial loads are generated and axial thrust from the turbine is minimized in operation. If, however, axial forces occur during operation, these are absorbed via two axial start-up linings (4), see Figure 4 (a), (c) and (d). For this purpose, pressure pieces with a spring-loaded ceramic ball are used to keep the friction as well as the damping of vibrations low. At the same time, this allows for a small heat input into the shaft. The turbine is supplied via the pressure line (5), see Figure 4 (c) and (d). The control of the test rig, i.e. the turbine, is achieved with a proportional pressure control valve, which is steplessly electronically controlled by means of a PC. Furthermore, M2 x 6 x 60° thread holes are provided at the front sides of the bearing shaft for the attachment of unbalance weights.

## 3 Experimental Analysis

### 3.1 Measurement Instrumentation

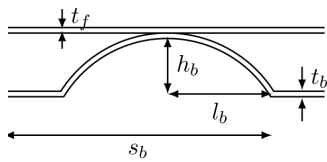
Referring to Figure 4 (a) and (b), for the rotordynamic analysis the vibration behavior at the front (F) and rear (R) bearing positions is measured in vertical and horizontal directions by means of two fiber-optic displacement sensors. The rotational speed is detected simultaneously by an infrared sensor (7). A black and white marking is therefore placed next to the turbine, see Figure 4 (b). Furthermore, the temperature at the bearing seat is measured by means of thermocouples of the type T, see Figure 4 (a).



**Figure 4:** Experimental setup: cross-sectional (a) view, (b) shaft, (c) view 1 and (d) view 2.

**Table 1:** Geometrical data of a GFB of the 1st generation (Manufacturer MSI.Inc).

Parameter	Value
Bearing radius $R$	19.050 mm
Bearing length $l$	38.100 mm
Bump-height $h_b$	0.50 mm
Bump-thickness $t_b$	0.1 mm
Bump-range $s_b$	4.572 mm
Number of bumps $N_b$	26
Half the length of a bump $l_b$	1.778 mm
Foil cover thickness $t_f$	0.1 mm
Elastic modulus $E$	$2.07 \times 10^{11}$ N/m <sup>2</sup>
Poisson's ratio $\nu$	0.3
Foil material	Inconel X-750



The sensors and the measurement instruments are listed in Table 3.

### 3.2 Test Procedure and Signal Processing

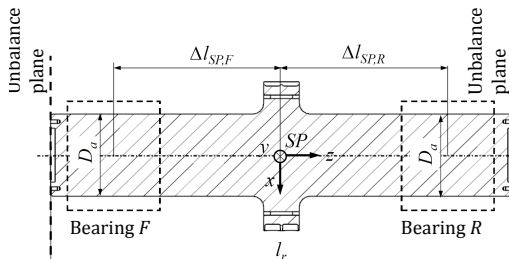
Two different experiments are carried out: first, the influence of the self-excitation is analyzed, see Figure 1, path 2. Hereto, the rotor is in the initial unbalanced state, i.e. no additional masses are attached to the balancing planes. According to DIN ISO 21940, a balance quality grade of G 0,4 is available. Second, the influence of the forced vibrations is investigated by different unbalance mass settings by means of static and couple unbalances. The

unbalance masses are listed in Table 4. This study is based on path 1 from Figure 1. Both studies are to demonstrate the classification shown in Figure 1. The tests are based on transient runs. For this purpose, the rotor is accelerated to its maximum rotational speed ( $n_{max} \approx 60\,000$  rpm). This state is held until stationary operation is established. Thereafter the pressurization of the turbine is switched off, the rotor decelerates and the measurement takes place. Excitations due to the flow through the turbine are thereby minimized. This procedure is performed more than 10 times to verify the reproducibility of the results. The reproducibility of experimental results is very good, so that an averaging of the results is not performed. The results of the transient rotordynamic analyses are shown in waterfall charts. Hereby, the magnitude of the pointer  $|r| = \sqrt{u^2 + v^2}$  of the displacement in  $x$ - and  $y$ -direction is plotted over the frequency component  $f$  and rotational speed  $n$ .

<sup>1</sup> Application field: tool spindle machines and propulsion of precision machines.

**Table 2:** Design data of the solid shaft

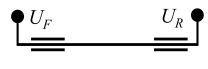

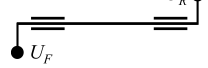
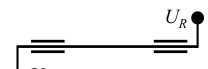

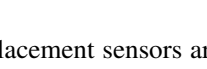
Parameter	Solid shaft
Material	42CrMo4 (1.7225)
Mass $m_r$	2.148 kg
Inertia $J_z$	568.425 mm <sup>2</sup> kg
Inertia $J_x, J_y$	6775.878 mm <sup>2</sup> kg
Rotor length $l_r$	212 mm
Bearing distance $\Delta l_{SP,F/R}$	72.5 mm
Shaft diameter (nominal) $D_a$	38 mm
Nominal gap bearing F $c_{0,F}$	55 $\mu\text{m} \pm 6 \mu\text{m}$
Nominal gap bearing R $c_{0,R}$	50 $\mu\text{m} \pm 6 \mu\text{m}$



**Table 3:** Measurement instrumentation of the rotordynamic experiment.

Sensor	Manufacturer	Type	Sensitivity/specification	Quantity
Rotational speed	Monarch	IRS- Infrared Sensor	1-999 999 min <sup>-1</sup>	1
Displacement	Philltec INC	RC 62	2.8 mV/ $\mu\text{m}$	4
Temperature	Omega	5TC-TT-KI-24-2M	Type T, max. 300 °C	10
PC-measurement electronics	NI	9215	AD-converter 16 Bit, $\pm 10$ V	3
PC-measurement electronics	NI	9213	16 channel thermocouple module 16 Bit	1
PC-measurement electronics	NI	cDAQ 9127	Measurement Chassis	1
PC-measurement electronics	NI	9162	Measurement Chassis	1

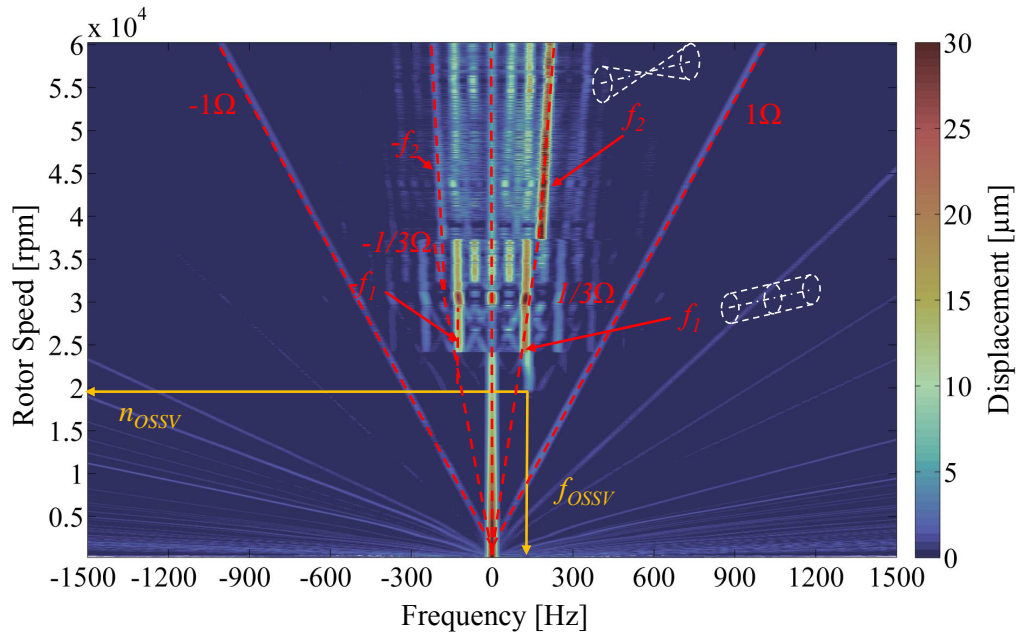
**Table 4:** Unbalance values of the rotor.

Rotor	Type of unbalance	Unbalance $U_F$	Unbalance $U_R$	
Solid shaft	static		0 gmm	0 gmm
			6 gmm	6 gmm
			12 gmm	12 gmm
	couple		0 gmm	0 gmm
			9 gmm	9 gmm
			12 gmm	12 gmm

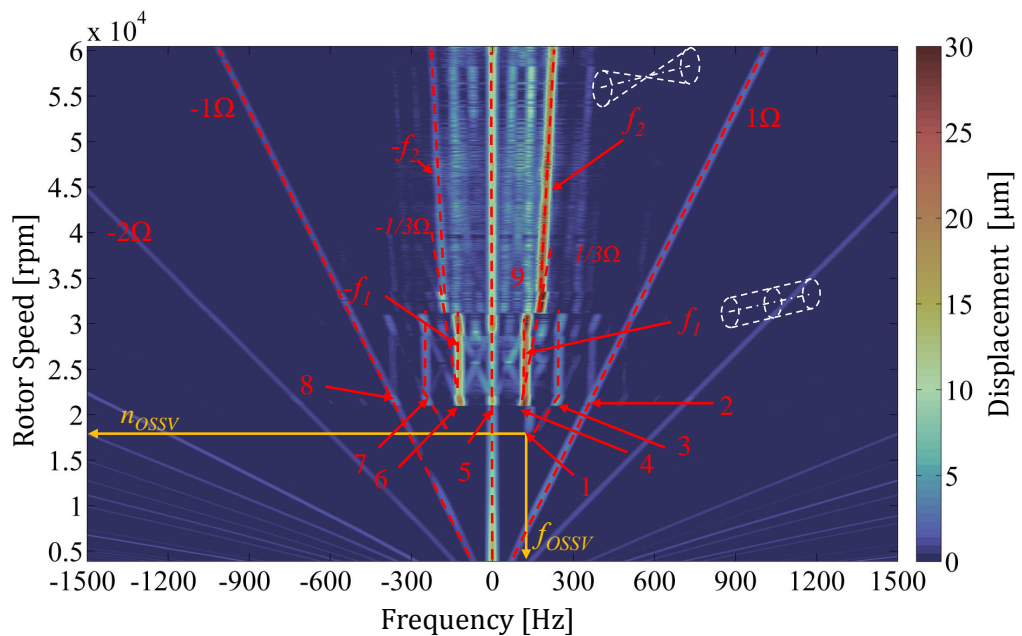
For this purpose, the time signals of the displacement sensors are sampled with 40 kHz and converted into the frequency domain by means of a Fast Fourier Transform (FFT). A digital Butterworth low-pass filter (cutoff frequency: 20 kHz) and a Hanning window are also used for frequency analysis. Possible amplitude damping, caused by signal processing, in particular resulting from the choice of the window, have been neglected, since the absolute values of the vibration amplitude are less of interest than their frequency characteristics. Due to the low temporal variance of the temperature, the sampling frequency of the thermocouples has been set to 100 Hz. The temperature of the bearing relative to the environment  $T_a$  is not expected to vary much during the study, since the bearing load is relatively low.

### 3.3 Experimental Results

#### 3.3.1 Assessment of the Self-excitation



(a) Run-up



(b) Coast-down

**Figure 5:** Waterfall charts of the solid shaft, measurement position: front bearing, (a) Run-up and (b) Coast-down

In Figure 5 the waterfall charts display the shaft displacement in forward and backward directions at the front

bearing (F) during (a) run-up and (b) coast-down. No additional unbalance is attached to the rotor. As a result, the nonlinear vibration behavior can be evaluated by means of a possible self-excitation by the gas film, see Figure 1 path 2. Figure 5 basically underlines that subharmonic vibrations start at the onset speed  $n_{OSSV}$  with the frequency  $f_{OSSV}$ . The results of the OSSV-point are summarized for the different measurements in Table 5. They reflect very well the behavior of the Duffing oscillator. During coast-down the OSSV is lower than during run-up. That reflects the Jump frequencies (C)-(D) respectively (A)-(B) in Figure 3. With the delayed onset of the subharmonic vibrations at higher rotational speeds of the run-up, a system with a positive feedback can be identified.

**Table 5:** OSSV at run-up and coast-down.

	Measurement cycle	$f_{OSSV}$	$n_{OSSV}$	Displacement amplitude $ r $
<b>Solid shaft</b>	Coast-down	136.72 Hz	17 754 rpm	2.698 $\mu\text{m}$
	Run-up	136.7 Hz	19 992 rpm	4.804 $\mu\text{m}$

### 3.3.2 Assessment of the nonlinear Vibrations

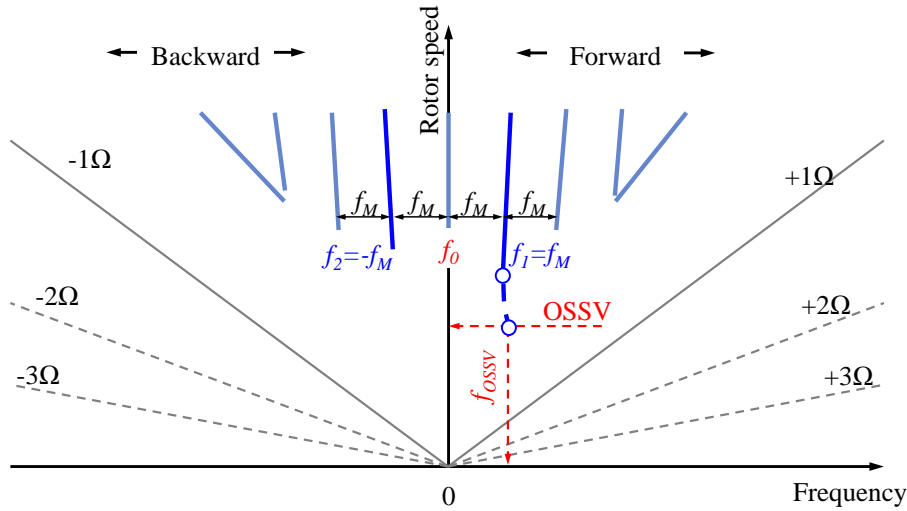
The waterfall chart in Figure 5 displays a variety of nonlinear vibrations as soon as the onset speed  $n_{OSSV}$  has been surpassed. In accordance with Figure 1, this is explained by the increased bearing shaft displacement due to the self-excitation. Thus, subharmonic vibrations are excited because of the existence of a positive feedback resulting from the progressive force-displacement-behavior. In Figure 5 (a), the frequency orders in forward and backward direction for  $\pm 1/3\Omega$  (indicated by dashed lines) induce the subharmonic resonance of the  $1/3\Omega$  order at the points (4) and (9). Behind the OSSV-point, the system oscillates in a self-excited manner synchronously with the first eigenfrequency  $f_1$ . This slightly detunes the system so that a slight jump close to point (4) towards lower frequencies occurs. The system is strongly dominated by the first eigenfrequency  $f_1$  (1st mode, cylindrical shape). At higher speeds, a further subharmonic resonance of the  $1/3\Omega$ -order occurs at point (9), which leads to a jump of the eigenfrequency  $f_2$  (2nd mode, cone shape). Furthermore, after the self-excitation and the nonlinear system behavior, a variety of combination frequencies, also known as frequency modulation, appears. For this purpose, Figure 6 (a) serves as an exemplary waterfall chart. In the case considered, self-excitation starts at the OSSV-point with the rotational speed  $n_{OSSV}$  and the frequency  $f_{OSSV}$ . Furthermore, the cylindrical mode  $f_1$  is strongly excited up from the point (4) by these nonlinear vibrations. If the frequency  $f_1$  up from point (4) is split between forward and backward motions and the half difference between backward and forward component is considered as the module frequency of action  $f_M = f_1$  (Equation 5). The value of half of the sum of the forward and backward component is considered as the carrier frequency  $f_c$  (Equation 5), the so-called side bands vibrate next to the main vibration components  $f_1$  due to the nonlinear feedback of the system. If a random frequency  $f$  is assumed, it may have higher and lower frequency side bands (index USB: upper side bands, index LSB: lower side bands). Kinetic energy will then be transferred from the basic vibration to the side bands. These side bands can, in combination with other frequencies, generate new frequencies according to the same scheme, see Figure 6 (a) and (b). The cascade-like modulation according to Figure 6 (b) can be calculated using Equation 3 and 4 for the side bands cf. Nguyen-Schäfer (2012).

$$f_{LSB} = \begin{cases} f_1 - 2f_M = f_c - f_M = f_2 \\ f_1 - 4f_M = f_c - 3f_M = 2f_2 - f_1 \\ f_1 - 6f_M = f_c - 5f_M = 3f_2 - 2f_1 \\ \dots \end{cases} \quad (3)$$

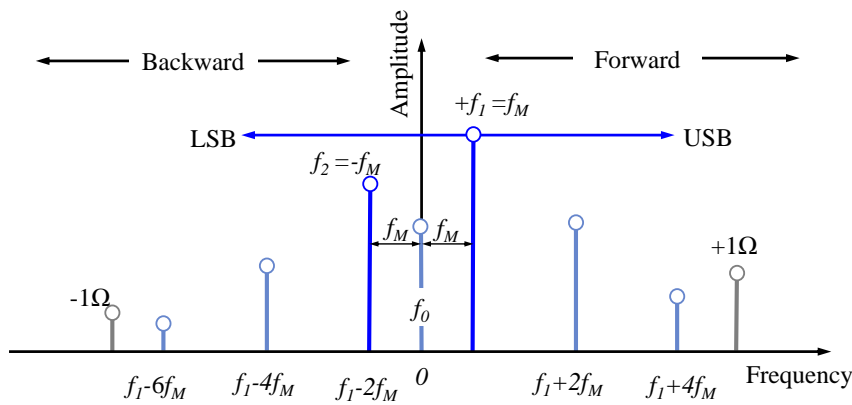
$$f_{USB} = \begin{cases} f_1 + 0f_M = f_c + f_M = f_1 \\ f_1 + 2f_M = f_c + 3f_M = 2f_1 - f_2 \\ f_1 + 4f_M = f_c + 5f_M = 3f_1 - 2f_2 \\ f_1 + 6f_M = f_c + 7f_M = 4f_1 - 3f_2 \\ \dots \end{cases} \quad (4)$$

$$f_M = \frac{1}{2}(f_1 - f_2) \quad f_c = \frac{1}{2}(f_1 + f_2) \quad (5)$$

Referring to the waterfall diagram of Figure 5 (b), combined frequency points (2-8) result. These points are summarized in Table 6. By applying Eq. (3) and (4) with the modulation frequency  $f_M = 117.19$  Hz of the point



(a) Waterfall chart



(b) Spectrum

**Figure 6:** Diagram of a frequency modulation: (a) in waterfall chart and (b) frequency spectrum with cascade-like frequency modulation.

(6) of Figure 5 (b), identical frequencies are calculated. This comparison further underlines the nonlinear system behavior, which is initiated by the onset of self-excitation at the OSSV point.

**Table 6:** Side band modulation of the waterfall chart of Figure 5 (b), solid shaft, coast-down with  $f_M = 117.19$  Hz.

Position	8	7	6	5	4	3	2
$f_i$	-351.56 Hz	-234.34 Hz	-117.19 Hz	0 Hz	117.18 Hz	234.375 Hz	351.56 Hz

### 3.3.3 Impact of Unbalance on the nonlinear Vibration Behavior

Path 1 is analyzed according to Figure 1 in order to prove the above hypothesis experimentally. The reason of nonlinear vibrations lies within forced vibrations due to a generally poorer balancing quality, so that nonlinear vibrations are generated even below the OSSV point. The unbalance values used are based on the data in Table 4. The results are plotted in the waterfall diagrams in Figures 7 and 8 for the cases of a static and couple unbalance. In principle, it can be stated: the higher the unbalance is, the more distinct a nonlinear rotor behavior due to the progressive force-displacement behavior of the bearing becomes. With exception of the 6 gmm measurement with static unbalance, see Figure 8 (a), subharmonic vibrations of the  $1/2\Omega$ -order occur as a result of the forced



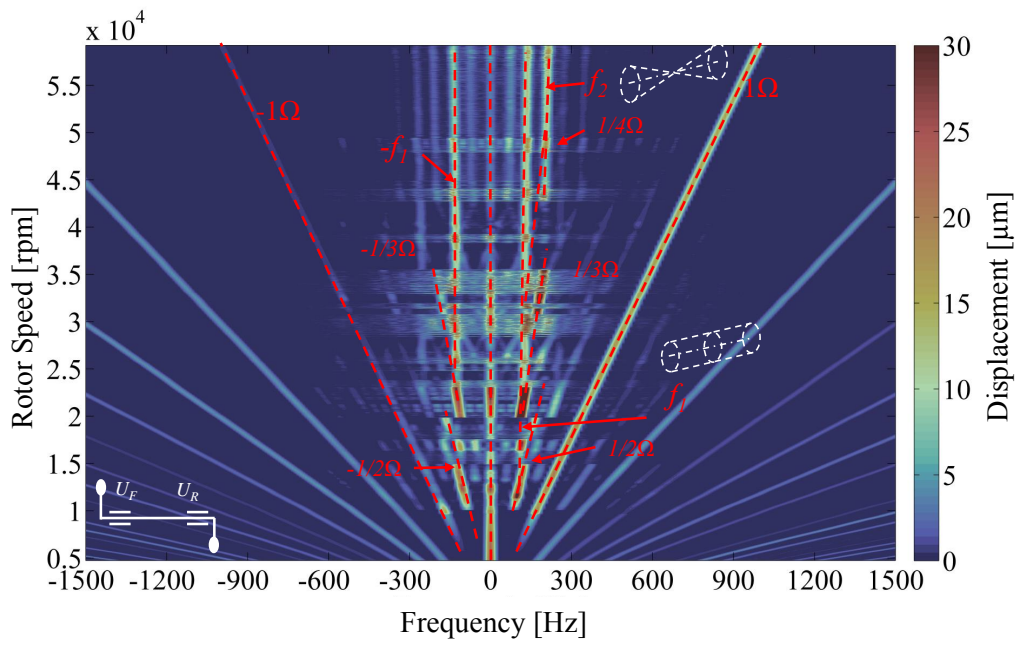
unbalance excitation already below the abovementioned OSSV point. The original unbalance state of the rotor has undergone little change by introducing this test mass, which is why the OSSV at 6 gmm is still present as a result of self-excitation. Subsequently,  $\pm 1/3\Omega$  and  $\pm 1/4\Omega$  orders are excited, which again implies the presence of a nonlinear system behavior due to the positive feedback and thus supports the hypothesis of the first path. Furthermore, the waterfall diagrams show that the second mode (cone shape) is strongly excited by the nonlinear oscillations  $\pm 1/3\Omega$  or  $\pm 1/4\Omega$  by means of the subharmonic resonances. The second mode oscillates with the frequency  $f_2$ .

In addition to the side bands, continuous spectral components are clearly visible in the case of the couple unbalance with  $U_i = 12$  gmm ( $i=F,R$ ). These can be chaotic, stochastic or non-steady-state vibrations, cf. Magnus et al. (2013). Above all, the latter effect is to be assumed, since the coast-down runs were very short in the experiments. This resulted in a heavily unsteady state regime. A detailed investigation of this effect was not carried out within the framework of the work, since these are not of great importance for the purpose of the work. Moreover, it can be observed, that the mass of the couple unbalance causes a stronger nonlinear behavior with higher vibration amplitudes compared to the static unbalance, see Figures 7 and 8. As a result of the couple unbalance and its kinematic effect on the rotor, the displacements close to the front (F) and rear (R) bearings are larger in comparison to those obtained in the static unbalance case. This is due to the conical mode, which is dominated by a forced vibration particularly in the operational range and it is sensitive to the present unbalance mass, according to the analysis in the Campbell diagram, see Figure 9. Unfortunately, the results for the higher couple unbalance case do not show the high conical mode vibrations. It was not possible to run the rotor in the relevant speed range due to the extremely high vibration level, see Figure 7 (b). A possible reason for this is the strong excitation of the rotor due to the unbalance and the subharmonic resonance, which excite the cone mode, thereby transferring the rotational kinetic energy of the drive into the translational vibrations. The drive power of the turbine is not sufficient in this case to accelerate the rotor to higher speeds.

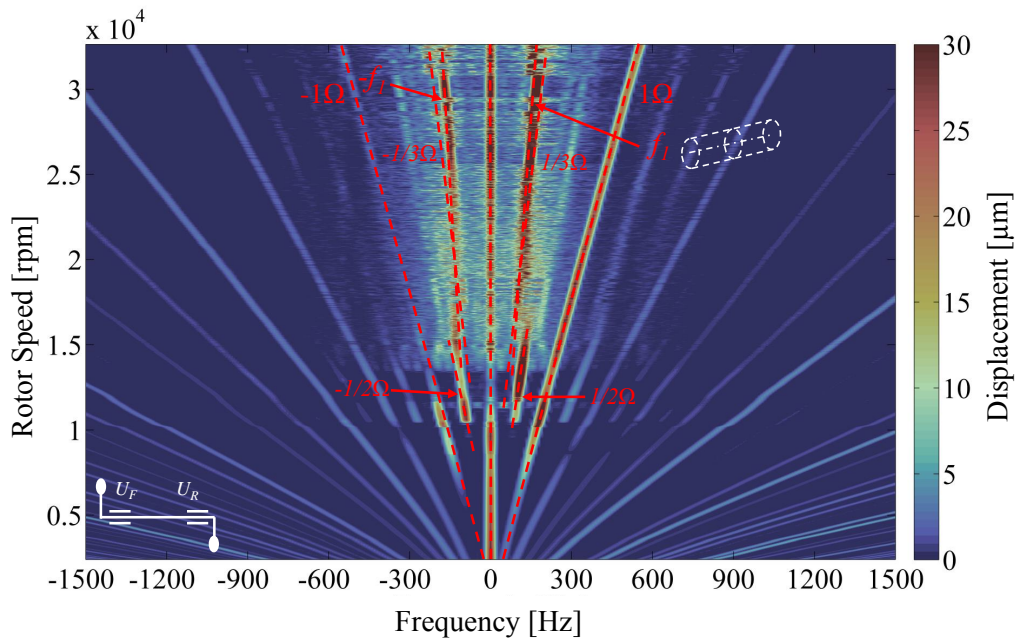
Based on the experimental results shown here, the path 1 of the classification of vibrations caused by driven vibration by a nonlinear progressive system is proven, whereby nonlinear vibrations occur before the self-excitation by the gas film, see Figure 1.

#### 4 Summary

In order to confirm the claimed vibration classification of this work a rigid rotor supported by two gas foil bearings is tested experimentally. The following results can be summarized: According to path 2, self-excited vibrations by the fluid film occur as a subharmonic *Whirl*-vibration at the OSSV-point. After the onset of subharmonic vibration, which developed synchronously with the 1st mode (cylindrical shape), a variety of subharmonic resonances of the  $\pm 1/3\Omega$  and  $\pm 1/4\Omega$  orders occurs due to the progressive force-displacement behavior. In addition to the unstable cylindrical mode (1st mode), these also excite the conical mode (2nd mode). According to path 1, the unbalance has a great influence on the nonlinear vibrations. A variety of subharmonic resonances and vibrations of the  $\pm 1/2\Omega$ ,  $\pm 1/3\Omega$  and  $\pm 1/4\Omega$  orders were identified as a result of the nonlinear progressive force-displacement behavior of the bearing. Even before self-excitation,  $\pm 1/2\Omega$  orders occur due to nonlinear behavior. In addition, a variety of frequencies are modulated by the nonlinear behavior.

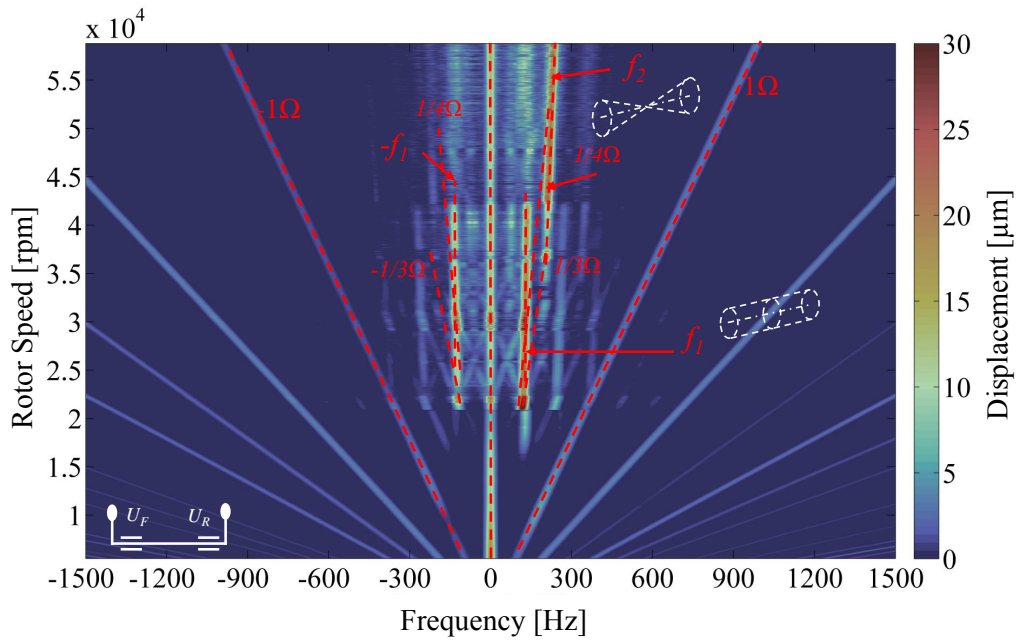


(a)  $U_i = 9 \text{ gmm}$  ( $i = F, R$ )

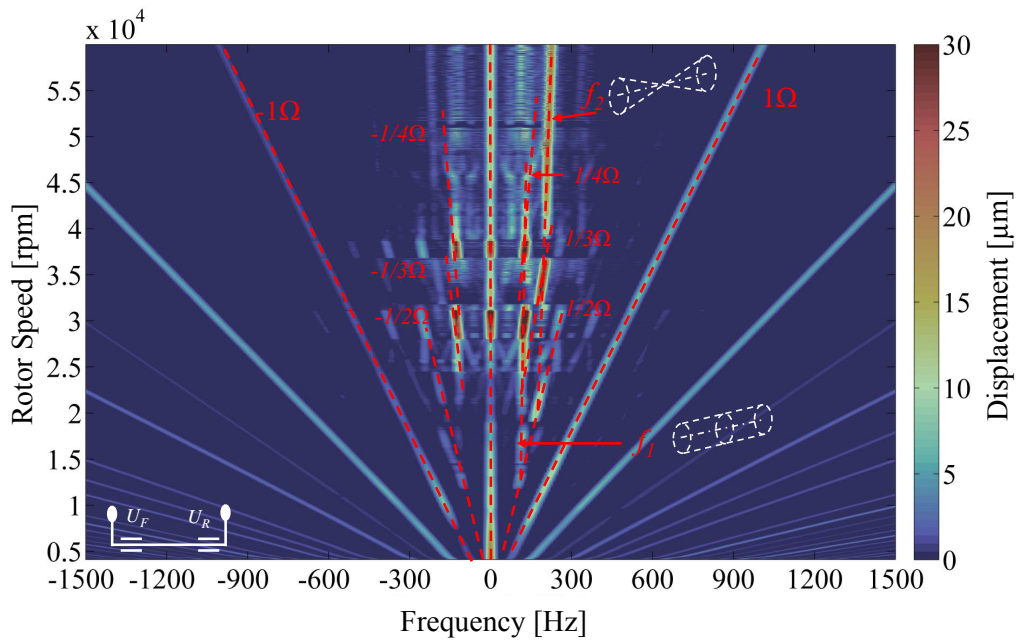


(b)  $U_i = 12 \text{ gmm}$  ( $i = F, R$ )

**Figure 7:** Couple unbalance on the solid shaft: waterfall charts (a) and (b) (measurement location: front bearing, coast-down).



(a)  $U_i = 6 \text{ gmm}$  ( $i = F, R$ )

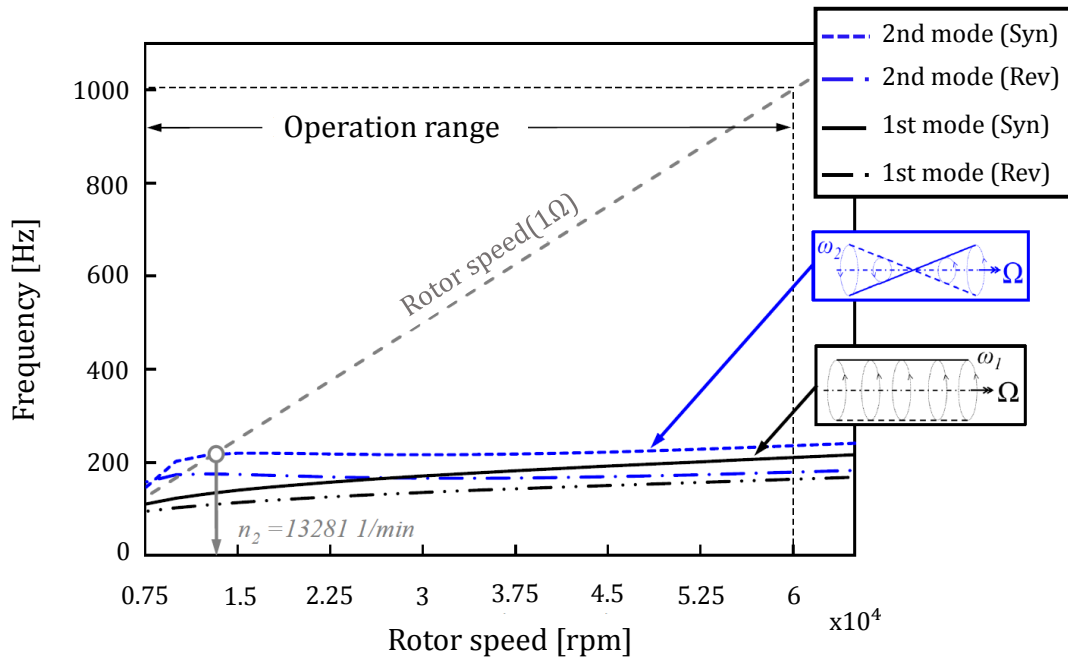


(b)  $U_i = 12 \text{ gmm}$  ( $i = F, R$ )

**Figure 8:** Static unbalance on the solid shaft: waterfall charts (a) and (b) (measurement location: front bearing, coast-down).

## 5 Appendix

### Eigenbehavior of the test rig in operation.



**Figure 9:** Campbell diagram of the solid shaft.

The following results are based on a rotordynamic model, which takes into account gyroscopic effects of the rotor as well as speed-dependent linearized stiffness and damping for the GFBs. The method for determining the linearized bearing parameters is given in Hoffmann et al. (2016); Hoffmann (2016). The forward and backward components of the two first modes in the operation range ( $n_{\max} = 60\,000 \text{ rpm}$ ) are displayed. Due to the very high-frequency bending modes, their critical speeds are not reached. In operation, according to this linear view, critical speeds  $n_2$  occur when there is a point of intersection between the spin speed line and the eigenfrequency of the 2nd mode (cone mode). This means that the rotationally synchronous excitation  $1\Omega$  is equal to the forward mode eigenfrequency  $f_2$  of the rotor. Backward whirls are neglected. The low-frequency cylindrical mode has no resonance for a synchronous excitation with  $1\Omega$  in operation above  $n = 7500 \text{ rpm}$ .

## References

- Balducchi, F.: *Analyse expérimentale des paliers et des butées aérodynamiques à feuilles*. Ph.D. thesis, Poitiers (2013).
- DellaCorte, C.; Valco, M. J.: Load capacity estimation of foil air journal bearings for oil-free turbomachinery applications. *Tribology Transactions*, 43, 4, (2000), 795–801.
- Dresig, H.; Rockhausen, L.; Holzweißig, F.: *Maschinendynamik*. Springer Berlin Heidelberg (2011).
- Heshmat, H.: Advancements in the performance of aerodynamic foil journal bearings: high speed and load capability. *Journal of Tribology*, 116, 2, (1994), 287–294.
- Heshmat, H.: Operation of foil bearings beyond the bending critical mode. *Journal of Tribology*, 122, 2, (2000), 478–479.
- Heshmat, H.; Shapiro, W.; Gray, S.: Development of foil journal bearings for high load capacity and high speed whirl stability. *Journal of Lubrication Technology*, 104, 2, (1982), 149–156.
- Hoffmann, R.: *Eine Methode für die Vorhersage nichtlinearer selbsterregter Schwingungen von Rotoren in Gasfolienlagern – Eine numerische und experimentelle Untersuchung*-. Ph.D. thesis, Technische Universität Berlin (2016).
- Hoffmann, R.; Munz, O.; Pronobis, T.; Barth, E.; Liebich, R.: A valid method of gas foil bearing parameter estimation: A model anchored on experimental data. *Proceedings of the Institution of Mechanical Engineers, Part C: Journal of Mechanical Engineering Science*, page 0954406216667966.
- Hoffmann, R.; Pronobis, T.; Liebich, R.: Non-linear stability analysis of a modified gas foil bearing structure. Proceeding: IFToMM 2010 - 9th International Conference on Rotor Dynamics, Milano, Italy (2014).
- Kim, K.-S.; Cho, B.-C.; Kim, M.-H.: Rotordynamic characteristics of 65 kw micro turbine with complaint air foil bearings. Proceeding: IFToMM 2010 - 8th International Conference on Rotor Dynamics, Seoul, Korea (2010).
- Kim, T. H.: *Analysis of side end pressurized bump type gas foil bearings: A model anchored to test data*. Ph.D. thesis, Texas A&M University, College Station (2007).
- Kovacic, I.; Brennan, M. J.: *The Duffing Equation: Nonlinear Oscillators and their Behaviour*. Wiley (2011).
- Larsen, J. S.: *Nonlinear analysis of rotors Supported by air foil journal bearings–theory and experiments*. Ph.D. thesis, Technical University of Denmark (2015).
- Magnus, K.; Popp, K.; Sestro, W.: *Schwingungen: Physikalische Grundlagen und mathematische Behandlung von Schwingungen*. Springer Fachmedien Wiesbaden (2013).
- Nguyen-Schäfer, H.: *Rotordynamics of automotive turbochargers: Linear and nonlinear rotordynamics–Bearing design–rotor balancing*. Springer (2012).
- San Andrés, L.; Kim, T. H.: Forced nonlinear response of gas foil bearing supported rotors. *Tribology International*, 41, 8, (2008), 704 – 715.
- San Andrés, L.; Rubio, D.; Kim, T. H.: Rotordynamic performance of a rotor supported on bump type foil gas bearings: Experiments and predictions. *Journal of Engineering for Gas Turbines and Power*, 129, 3, (2007), 850–857.
- Sim, K.; Lee, Y.-B.; Kim, T. H.; Lee, J.: Rotordynamic performance of shimmed gas foil bearings for oil-free turbochargers. *Journal of Tribology*, 134, 3, (2012), 031102–1–031102–11.
- Yamamoto, T.; Ishida, Y.: *Linear and Nonlinear Rotordynamics: A Modern Treatment with Applications*. A Wiley-Interscience publication, Wiley (2001).

---

Address: Chair Engineering Design and Product Realiability, TU Berlin, Germany  
email: gervais.c.djokokayo@campus.tu-berlin.de